MIT Open Access Articles

Detection of helium bubble formation at fcc-bcc interfaces using neutron reflectometry

Massachusetts Institute of Technology

Detection of helium bubble formation at fcc-bcc interfaces using neutron reflectometry

A. Kashinath, P. Wang, J. Majewski, J. K. Baldwin, Y. Q. Wang et al.

Detection of helium bubble formation at fcc-bcc interfaces using neutron reflectometry

A. Kashinath,[1] P. Wang,[2] J. Majewski,[2] J. K. Baldwin,[3] Y. Q. Wang,[4] and M. J. Demkowicz[1]

[1]*Department of Materials Science and Engineering, Massachusetts Institute of Technology, Cambridge, Massachusetts 02139, USA*
[2]*Lujan Neutron Scattering Center, Los Alamos National Laboratory, Los Alamos, New Mexico 87545, USA*
[3]*Center for Integrated Nanotechnologies, Materials Physics and Application Division,*
Los Alamos National Laboratory, Los Alamos, New Mexico 87545, USA
[4]*Materials Science and Technology Division, Los Alamos National Laboratory, Los Alamos,*
New Mexico 87545, USA

We use neutron reflectometry to find the critical helium (He) fluence required to form He bubbles at interfaces between fcc and bcc metals. Our findings are in agreement with previous experimental as well as modeling results and provide evidence for the presence of stable He platelets at fcc-bcc interfaces prior to bubble formation. The stable storage of He in interfacial platelets may provide the basis for the design of materials with increased resistance to He-induced degradation. © 2013 AIP Publishing LLC. [http://dx.doi.org/10.1063/1.4813780]

I. INTRODUCTION

Management of implanted Helium (He) is crucial to the development of new fusion and fission reactor materials.[1,2] Because of its insolubility in crystalline metals,[3] implanted He immediately precipitates out into 2–3 nm diameter bubbles.[4] Unlike He-free cavities, these bubbles are thermodynamically stable and are effective nuclei for the growth of larger voids, which in turn accelerate radiation-induced swelling[5–7] and high-temperature embrittlement of grain boundaries.[8–10]

The current approach to reducing the deleterious effects of He in structural materials is based on delaying the so-called "bubble-to-void" transition.[11,12] By reducing the concentration of radiation-induced vacancies and increasing the density of bubble nucleation sites, the critical fluence of implanted He required to transform stable bubbles into voids may be maximized.[13] Nanoferritic alloys (NFAs), such as oxide dispersion strengthened (ODS) steels, are one class of materials that have been designed to be resistant to He-induced damage based on this principle. These alloys contain a high density of nanometer-scale Y-Ti-O precipitates that increase the recombination rate of radiation-induced point defects (thereby reducing vacancy supersaturation) and partition implanted He to numerous disconnected trapping sites at the interfaces between oxide particles and their Fe-base matrix, giving rise to numerous small, stable bubbles.[14,15]

Similar to NFAs, some multilayer nanocomposites of face-centered cubic (fcc) and body-centered cubic (bcc) metals also contain heterophase interfaces that are excellent trapping sites for He. Furthermore, in magnetron sputtered Cu-Nb, Cu-Mo, and Cu-V multilayers, no He bubbles may be detected under transmission electron microscopy (TEM) up to He concentrations of several atomic percent:[4,16–18] orders of magnitude higher than the bulk solubility limit in pure metals.[3] The delayed formation of He bubbles in these materials is attributed to the stable storage of implanted He at

their fcc-bcc interfaces. The critical interfacial He concentrations needed to observe bubbles is consistent with trapping of He at misfit dislocation intersections (MDIs)[19,20]—specifically, ~25 He atoms/MDI—without bubble formation.[21]

Multiscale modeling has shown that the delayed formation of He bubbles at fcc-bcc interfaces is due to storage of He in stable nanometer-scale platelet-shaped clusters at MDIs.[22] As these platelets absorb further He atoms, they undergo a "platelet-to-bubble" transformation (analogous to the classical "bubble-to-void" transformation[11,12]), accompanied by a three-fold increase in their volume. This dramatic increase in volume is a consequence of a change in growth mode of interfacial He clusters, from platelets that wet the interface to bubbles that do not. These resulting He-filled bubbles may be seen in TEM, but the nanoscale platelets from which they are predicted to form are too small to resolve by TEM. It is therefore unclear from TEM alone whether the formation of interfacial He bubbles is indeed preceded by the storage of He in platelets or if, at low He concentrations, fcc-bcc interfaces contain regular He-filled bubbles that are simply too small to resolve by TEM. Thus, there is a need to identify the "platelet-to-bubble" transition *via* other techniques. Neutron reflectometry (NR) is well-suited to this task since it is sensitive to local density changes induced by He trapped at interfaces.[23] Additionally, unlike ion-beam analysis methods such as elastic recoil detection[24] or nuclear reaction analysis,[25] NR has near Å-level depth resolution, which allows density changes to be attributed unambiguously to specific locations within the samples under investigation.

We use NR to characterize magnetron sputtered fcc-bcc bilayers that have been implanted with He and find that no detectable He-induced changes occur until a critical He fluence is exceeded, whereupon regions of reduced density localized at the fcc-bcc interfaces are observed. This critical He fluence depends on the structure of the fcc-bcc interfaces: it is proportional to the areal density of MDIs they contain.

114, 043505-1

These findings are consistent with the multiscale modeling prediction[22] that He at fcc-bcc interfaces is initially stored in the form of stable platelets that transform into He-filled bubbles of higher volume at sufficiently large He fluences.

II. EXPERIMENTAL PROCEDURE AND DATA ANALYSIS

A. Deposition of fcc-bcc bilayers and He ion implantation

The interfaces studied here are formed between a fcc metal—copper (Cu)—and one of three bcc metals: niobium (Nb), molybdenum (Mo), or vanadium (V). Each fcc-bcc interface is deposited as a bilayer, with nominal layer thicknesses of 20 nm, on a silicon (Si) substrate using magnetron sputtering at the Center for Integrated Nanotechnologies (CINT), Los Alamos National Laboratory. The depositions are carried out at room temperature in an argon atmosphere at a pressure of 6 mTorr and a 10 cm substrate-to-target distance. The vacuum chamber is evacuated to a base pressure lower than 5×10^{-8} Torr prior to deposition. The crystallographic character of interfaces in all three types of magnetron sputtered fcc-bcc bilayers is identical: all form along closest packed planes in the adjacent crystals ($\{111\}_{fcc}\|\{110\}_{bcc}$) in the Kurdjumov-Sachs orientation ($\langle110\rangle_{fcc}\|\langle111\rangle_{bcc}$).[26]

After deposition, samples are implanted at room temperature with 20 keV ^{4}He$^+$ ions using the 200 kV Varian ion implanter at the Ion Beam Materials Laboratory (IBML) at Los Alamos National Laboratory. Cu-Nb bilayer samples are implanted to seven different fluences: 5×10^{15}/cm^2, 10^{16}/cm^2, 2×10^{16}/cm^2, 3×10^{16}/cm^2, 4×10^{16}/cm^2, 5×10^{16}/cm^2, and 10^{17}/cm^2. Cu-Mo and Cu-V bilayer samples are implanted to two different fluences: 5×10^{15}/cm^2 and 10^{16}/cm^2. Implantation to each fluence is carried out on separate samples.

During implantation, the beam current is held at a nominal value of $2\,\mu$A/cm^2 (or at the helium ion flux of 1.25×10^{13} ions/cm^2/s) to limit the heating of the sample due to the incident beam. The depth profile of He implanted under these conditions in Cu-Nb is calculated using Stopping and Range of Ions in Matter (SRIM),[27] as shown in Figure 1. This calculation reveals that only $\sim$8.7% of the implanted He ions are deposited in either the Cu or the Nb layer of the sample. The remaining He atoms are deposited in the Si substrate. Similarly, in the Cu-Mo and Cu-V samples, only $\sim$8.1% and $\sim$6.2% of the implanted He ions are deposited in the metal bilayer while the rest penetrates into the Si substrate.

B. Neutron reflectometry measurements of He-ion implanted fcc-bcc bilayers

NR measurements on the He implanted fcc-bcc bilayer samples are carried out at the Surface Profile Analysis Reflectometer (SPEAR), a time-of-flight (ToF) instrument at the Lujan Neutron Scattering Center, Los Alamos National Laboratory.[28] The neutron beam is produced from a spallation source and, after moderation by liquid H$_2$, is directed onto the sample at a very low angle while the specular reflection is recorded by a ToF, position-sensitive detector.
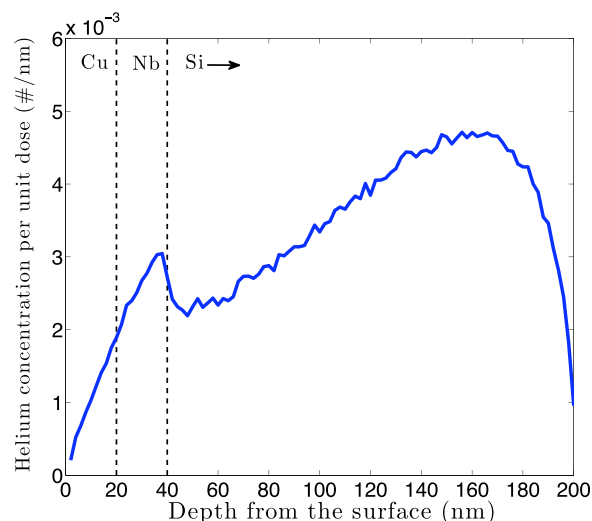

FIG. 1. Depth profile of 20 keV He ions implanted into a Cu-Nb bilayer with individual layer thicknesses of 20 nm on a Si substrate calculated using SRIM.

Reflectivity is defined as the ratio of the intensity of the reflected beam to the incident beam and is a function of the neutron momentum transfer vector Q_z, where $Q_z = 4\pi \sin(\theta)/\lambda$, θ is the angle of incidence of the beam, and λ is the wavelength of the neutron. In our ToF NR measurements, the neutron wavelength range varies from 4.5 to 16 Å. For the data presented in this manuscript, NR for the entire Q_z-range is covered by measurements performed at 3 different angles of incidence (i.e., $\sim$0.5°, $\sim$1.0°, $\sim$2.6°), and subsequently the reflectivity curves are combined together. The specular scattering, averaged over the area of the neutron beam footprint ($\sim$500 mm^2), is analyzed to extract the scattering length density (SLD) profile as a function of depth from the sample surface.

The SLD of a volume V containing n different atom types may be expressed as

$$SLD = \frac{1}{V} \sum_{i=1}^{n} b_i, \tag{1}$$

where b_i is the coherent scattering length of the ith atom type. Knowing the SLD profile as a function of depth, information about the thickness, density, chemical composition, and roughness of each layer in the bilayer sample may be estimated. Since b_i is not a monotonic function of atomic number,[29] the neutron scattering contrast between Cu and Nb, Mo, and V is sufficient to study He-implanted fcc-bcc bilayers with sub-nanometer precision.

C. NR data interpretation and uncertainty estimation

The reflectivity curve, measured by NR, depends on the SLD profile in the direction perpendicular to the sample surface. The structure of the He-implanted fcc-bcc bilayers is approximated by a layered slab model parameterized by the thickness, SLD, and top interface roughness. The model consists of metal layers sandwiched between a super-phase (air) and a sub-phase (Si). We account for the thin native oxide layer that forms on the Si substrate. Tabulated SLD values[30]

for the Si substrate, SiO_2, Cu, Nb, Mo, and V are used in the model. Given a trial SLD profile, the Abeles matrix method[31,32] as implemented in Motofit[33] may be used to calculate the corresponding reflectivity curve. The model is then refined to minimize the χ^2 value—a measure of the goodness of fit[34]—between the calculated and measured reflectivity curves by changing the parameters that describe each layer. To avoid over-fitting, simple structural models employing the minimum number of layers to obtain satisfactory fits are used.

Once a best-fit set of model parameters is achieved, the uncertainties of these parameters may also be quantified by measuring the increase in χ^2 that comes about from perturbing each individual fitting parameter. We define $\tilde{\chi}^2$ as the deviation of the reflectivity calculated using the perturbed parameter values from the best-fit reflectivity

$$\tilde{\chi}^2 = \sum_{i=1}^{N} \left(\frac{y_i^{bf} - y_i^{p}}{y_i^{bf}} \right)^2. \qquad (2)$$

Here, y_i^{bf} is the best-fit to the measured reflectivity, y_i^{p} is the reflectivity value obtained by perturbing one parameter of the structural model, and N is the number of data points. The uncertainties on the fitting parameters are bounds within which $\tilde{\chi}^2$ is 5% or less.

Upper and lower bounds on best-fit SLD profiles are estimated by superimposing the upper and lower bounds for each individual fitting parameter. All SLD profiles with $\tilde{\chi}^2$ less than or equal to 5% are contained within these bounds but the converse is not true: not all SLD profiles within these bounds have $\tilde{\chi}^2$ less than or equal to 5%. Therefore, our uncertainty estimates for best-fit SLD profiles are conservative.

III. RESULTS FROM THE NEUTRON SCATTERING EXPERIMENTS

A. He-implanted Cu-Nb bilayers

Raw NR data, best-fit reflectivity curves, and corresponding SLD profiles for Cu-Nb bilayers implanted with increasing fluences of He ions are presented in Figure 2. The thickness of the SLD profiles reflects the conservative uncertainty bounds computed by the method described in Sec. II C. The Cu-Nb interface is located at the origin in all of the SLD profiles. The fitted model parameters and their uncertainties for the He implanted Cu-Nb bilayers are summarized in Table I.

At the lowest He ion implantation fluence of 5×10^{15}/cm^2, the best-fit SLD profile (Figure 2(a)) is a Cu-Nb bilayer with a sharp and well-defined interface between fully dense Cu and Nb. Increasing the implanted He fluence to 3×10^{16}/cm^2 does not lead to any change in the inferred mass density of either the Cu or Nb layer nor in the sharpness of the interface between them (Figures 2(b)–2(d)). Differences in the thickness of individual Cu and Nb layers in Figs. 2(a)–2(d) are due to inherent variability in the magnetron sputtering process.

At a He fluence of 4×10^{16}/cm^2, however, the Cu-Nb bilayer structure is significantly altered. The intensity of the reflected neutron beam near $Q_z = 0.05 \, \text{Å}^{-1}$ (indicated by
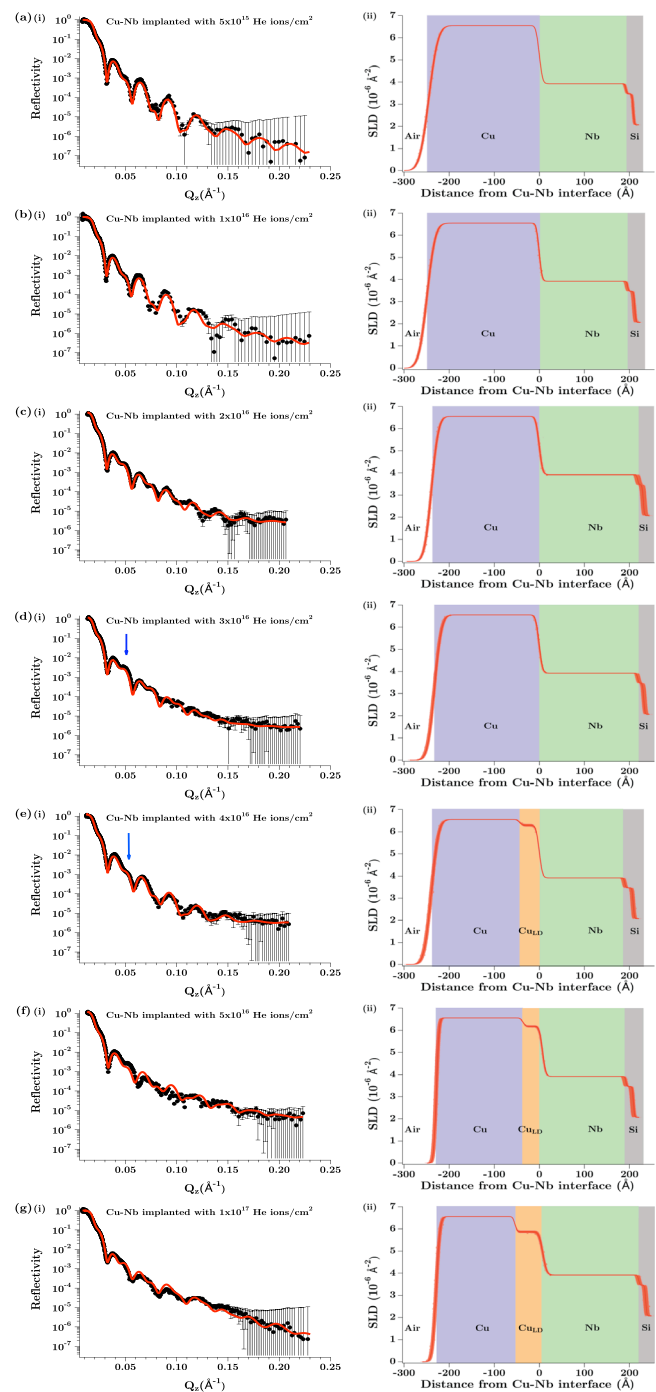

FIG. 2. (a)-(g)(i) NR data (filled circles) from He implanted Cu-Nb bilayer samples and fitted curves (solid red lines). The error bars denote the standard deviation for each NR measurement. (a)-(g)(ii) SLD profiles from which the NR fits are obtained along with schematics of their interpretation in terms of composition. The width of the SLD profile indicates the uncertainty in structural parameters. Blue arrows in (d) and (e) indicate the feature at $Q_z = 0.05 \, \text{Å}^{-1}$ that undergoes a decrease in reflectivity when the He fluence is increased from 3×10^{16}/cm^2 to 4×10^{16}/cm^2.

blue arrows in Figs. 2(d) and 2(e)) decreases appreciably at this fluence. To account for the reflectivity data, a new layer of SLD slightly lower than that of Cu must be included at the Cu-Nb interface. As will be discussed in Sec. IV A, we interpret this layer as consisting of Cu with a reduced mass density. Thus, we label the layer as "Cu$_{LD}$" (low density Cu) in Figure 2(e). SLDs in the Cu layer further from the interface

TABLE I. Model parameters used to fit NR data for He-implanted Cu-Nb bilayers.

	Layer (from air)	Thickness (Å)	SLD (10^{-6} Å^{-2})	Roughness (Å)
He fluence: 5×10^{15}/cm^2	Cu	245.1 ± 3.6	6.55	16.2
	Nb	191.89 ± 3.2	3.92	5.9
	SiO$_2$	16.34	3.47	2
He fluence: 10^{16}/cm^2	Cu	249.15 ± 4.6	6.55	14.7
	Nb	195.63 ± 4.1	3.92	5.2
	SiO$_2$	15.84	3.47	2
He fluence: 2×10^{16}/cm^2	Cu	239.07 ± 4.9	6.55	12.4
	Nb	218.23 ± 5.3	3.92	6.2
	SiO$_2$	12.29	3.47	2
He fluence: 3×10^{16}/cm^2	Cu	232.48 ± 5.8	6.55	12.4
	Nb	219.23 ± 4.6	3.92	6.1
	SiO$_2$	13.34	3.47	2
He fluence: 4×10^{16}/cm^2	Cu	196.11 ± 5.2	6.55	12.7
	Cu$_{LD}$	42.55 ± 3.2	6.29 ± 0.07	4.8
	Nb	189.29 ± 5.9	3.92	5.9
	SiO$_2$	18.84	3.47	2
He fluence: 5×10^{16}/cm^2	Cu	192.46 ± 4.7	6.55	4.7
	Cu$_{LD}$	44.55 ± 2.8	6.18 ± 0.05	4.8
	Nb	184.29 ± 4.8	3.92	5.7
	SiO$_2$	16.77	3.47	2
He fluence: 10^{17}/cm^2	Cu	175.01 ± 4.3	6.55	6.9
	Cu$_{LD}$	62.06 ± 3	5.87 ± 0.06	4
	Nb	212.72 ± 3.6	3.92	7.2
	SiO$_2$	15.84	3.47	2

TABLE II. Model parameters used to fit NR data for He-implanted Cu-Mo bilayers.

	Layer (from air)	Thickness (Å)	SLD (10^{-6} Å^{-2})	Roughness (Å)
He fluence: 5×10^{15}/cm^2	Cu	240.02 ± 5	6.55	12.3
	Mo	235.07 ± 5.7	4.33	5.2
	SiO$_2$	12.69	3.47	2
He fluence: 10^{16}/cm^2	Cu	180.06 ± 4.8	6.55	12.8
	Cu$_{LD}$	43 ± 2	6.35 ± 0.14	5.3
	Mo	233.07 ± 4.2	4.33	4.6
	SiO$_2$	17.69	3.47	2

and corresponding SLD profiles. The best-fit parameters are presented in Table II. The SLD profile of the Cu-Mo bilayer implanted with He to a fluence of 5×10^{15}/cm^2 (Figure 3(a)) contains two layers—Cu and Mo—with a sharp interface between them. When the He fluence is doubled to 10^{16}/cm^2, the best-fit SLD profile (Figure 3(b)) reveals a reduced SLD layer at the interface between Cu and Mo, which we again label as Cu$_{LD}$.

NR measurements and SLD fits for He-implanted Cu-V bilayers are presented in Figure 4 while corresponding fitting parameters are given in Table III. At a He fluence of 5×10^{15}/cm^2, the SLD of the bilayer shows distinct Cu and V regions (Figure 4(a)). When the He implantation fluence is increased to 10^{16}/cm^2, a distinct Cu$_{LD}$ layer is additionally found at the interface between Cu and V (Figure 4(b)).

IV. DATA INTERPRETATION AND ANALYSIS

A. Interpretation of reduced SLD interfacial layers

As demonstrated in Figures 2–4, He implantation above a critical fluence causes the formation of a distinct layer inside the Cu adjacent to fcc-bcc interfaces with SLD somewhat lower than that of pure Cu. Several potential explanations of this finding were considered. One possibility is that the observed change in SLD is due to an additional NR

and in the Nb layer remain unaltered. At the lowest implanted He fluence where a Cu$_{LD}$ layer is seens, 4×10^{16}/cm^2, the Cu$_{LD}$ layer is 42.5 Å thick and has a SLD of 6.289×10^{-6} Å^{-2}, slightly smaller than that of pure Cu.[30] As the implanted He fluence increases, the SLD of Cu$_{LD}$ decreases, and its thickness increases as shown in Figs. 2(f) and 2(g).

B. He-implanted Cu-Mo and Cu-V bilayers

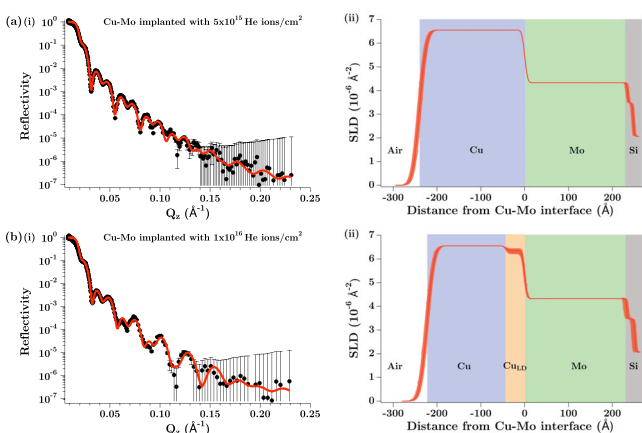Figure 3 shows raw NR reflectivity data from He implanted Cu-Mo bilayer samples along with best-fit curves

FIG. 3. (a)-(b)(i) NR data (filled circles) from He implanted Cu-Mo bilayer samples and fitted curves (solid red lines). The error bars denote the standard deviation for each NR measurement. (a)-(b)(ii) SLD profiles from which the NR fits are obtained along with schematics of their interpretation in terms of composition. The width of the SLD profile indicates the uncertainty in structural parameters.

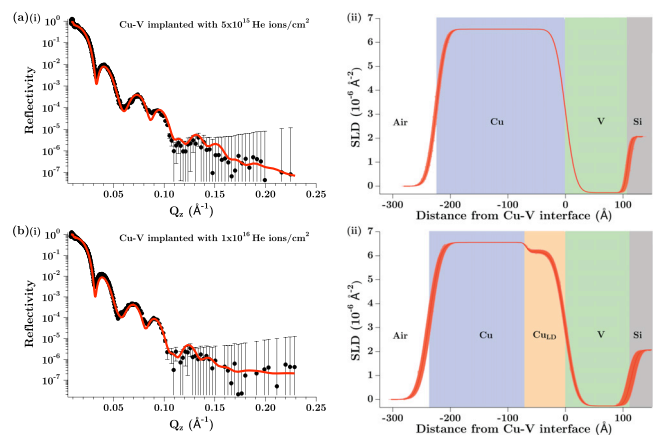FIG. 4. (a)-(b)(i) NR data (filled circles) from He implanted Cu-V bilayer samples and fitted curves (solid red lines). The error bars denote the standard deviation for each NR measurement. (a)-(b)(ii) SLD profiles from which the NR fits are obtained along with schematics of their interpretation in terms of composition. The width of the SLD profile indicates the uncertainty in structural parameters.

TABLE III. Model parameters used to fit NR data for He-implanted Cu-V bilayers.

	Layer (from air)	Thickness (Å)	SLD (10^{-6} Å^{-2})	Roughness (Å)
He fluence: 5×10^{15}/cm^2	Cu	224.37 ± 4.5	6.55	12.9
	V	108.05 ± 5	-0.271	14.3
He fluence: 10^{16}/cm^2	Cu	169.04 ± 4	6.55	15.3
	Cu$_{LD}$	68 ± 3.1	6.16 ± 0.09	4.4
	V	114.32 ± 4	-0.271	15.6

signal from implanted He ions that have been trapped at the interfaces. Several modeling studies have shown that fcc-bcc interfaces are indeed excellent traps for He.[22,35] However, since He has a positive SLD,[30] incorporation of He into the interface without a concomitant decrease in the density of the surrounding material would give rise to a net increase in SLD, rather than a reduction.

Furthermore, according to the SRIM calculations discussed in Sec. II A, at any given total fluence, comparable amounts of He may be expected to be trapped at interfaces in all three bilayer types. However, layers of reduced SLD are detected in Cu-Mo and Cu-V at implanted He fluences approximately four times smaller than in Cu-Nb. There is no reason to suspect that NR would be more sensitive to He in Cu-Mo and Cu-V than to He in Cu-Nb. Therefore, we conclude that the appearance of a layer of reduced SLD is not due to an additional NR signal directly from the implanted He. Furthermore, since no changes in bilayer structure are detected below the critical fluence required to form layers of reduced SLD, we also conclude that the NR measurements described here are not able to directly detect implanted He. This may be explained by the low scattering density of He compared to Cu, Nb, and Mo and its relatively low atomic concentration, even at the highest fluences used in this study.

Another potential interpretation of the low SLD interface layer is mixing of impurity bcc atoms into the neighboring Cu layer. Since Nb, Mo, and V have lower SLD values than Cu, this mechanism could account for a reduction of SLD. Nevertheless, several arguments militate against this interpretation. All of the fcc-bcc pairs used in this study have extremely low solid solubilities and do not form intermetallic compounds. Thus, in thermodynamic equilibrium, interfaces between them are atomically sharp.

Ion-induced mixing may force mutually insoluble elements into supersaturated solution, but requires the impinging ion to have a comparable atomic mass to that of the target atoms.[36] However, the ratio of the atomic mass of He to those of Cu, Nb, Mo, and V is low, so significant ion-induced mixing is not expected in this study. Indeed, previous investigations have confirmed that Cu-Nb interfaces remain atomically sharp, even when implanted with higher energy He ions than the ones used here.[37,38]

It is furthermore not clear how ion-induced mixing could give rise to the threshold He fluences required for the formation of reduced SLD layers. Moreover, previous investigations of ion-induced mixing in Cu-Mo and Cu-Nb bilayers have shown a greater tendency for mixing in the

latter than in the former,[39] in contrast to the higher He fluence required to form reduced SLD layers in Cu-Nb than in Cu-Mo. In view of the foregoing arguments, we conclude that impurity bcc atoms are not responsible for the formation of the reduced SLD layers found in this study.

Finally, the SLD reduction in regions adjacent to fcc-bcc interfaces may be due to a decrease in the average mass density of Cu upon the formation of He-filled bubbles there. Both modeling and experimental investigations on Cu-Nb have confirmed that such bubbles tend to grow into the Cu layer, rather than into the adjacent bcc layer.[40] Furthermore, the threshold He fluence required to form layers of reduced SLD may be explained by the discrete "platelet-to-bubble" transformation recently predicted by multiscale modeling.[22]

In this interpretation, below the critical implantation fluence, He atoms deposited in the bilayer are trapped in stable platelet-shaped, nanometer-scale clusters at the fcc-bcc interfaces. Because the size of the interfacial He platelets is comparable to the depth resolution limit of NR, the SLD profile of the bilayers is unchanged below the critical fluence. With increasing He fluence, the number of He atoms trapped in each interfacial platelet increases until it reaches a threshold value, beyond which it transforms into approximately spherical He-filled bubbles. This "platelet-to-bubble" transformation is accompanied by an approximately three-fold increase in the volume of the He-filled cavity and produces a decrease in mass density of Cu detectable by NR.

In addition to the qualitative reasons given above, two quantitative arguments support the hypothesis that the layers of reduced SLD found here are indeed regions where the average density of Cu has decreased due to a platelet-to-bubble transformation. These arguments are described in the following subsections. Henceforth, we refer to the layers of reduced SLD as layers of low density Cu: Cu$_{LD}$.

B. Critical He fluence for platelet-to-bubble transformation

At the Cu-Nb interface, Cu$_{LD}$ layers form when the implanted He fluence is between 3×10^{16}/cm^2 and 4×10^{16}/cm^2. In the case of Cu-Mo and Cu-V, the critical fluence lies in the range 5×10^{15}/cm^2–10^{16}/cm^2. These fluence ranges may be directly related to the areal densities of MDIs present in the semi-coherent fcc-bcc interfaces studied here. MDIs are trapping sites for He, each of which is thought to be capable of storing 20–25 He atoms in stable nanoscale interfacial platelets.[21,22] The areal density of MDIs is determined by the lattice mismatch across the interface and decreases as Cu-Nb > Cu-Mo > Cu-V.

As described in Sec. II A, only a fraction of the total implanted He fluence ends up in the fcc-bcc bilayers, the remainder being implanted into the underlying Si substrate. This fraction differs for the three fcc-bcc pairs investigated here. For the average Cu-Nb bilayer thickness estimated from NR measurements, SRIM[27] calculations show that $9.3 \pm 1.5\%$ of the implanted He ends up in either Cu or Nb layer. In the Cu-Mo and Cu-V bilayer samples, only $11.8 \pm 1.7\%$ and $4.1 \pm 0.8\%$ of the implanted He is deposited in the fcc and bcc layers, respectively. To make a

quantitative comparison between the critical He fluences for Cu_{LD} layer formation and areal densities of MDIs, these differences must be accounted for. We define a reduced fluence, d_R, as the product of the total implanted He fluence, d, and the fraction, f, of the total fluence that ended up in the fcc and bcc layers

$$d_R = d \times f. \qquad (3)$$

Figure 5 plots the reduced critical He fluences required to detect Cu_{LD} layers in Cu-Nb, Cu-Mo, and Cu-V interfaces using NR as a function of the lattice parameter ratios a_{bcc}/a_{fcc} of these fcc-bcc pairs. Also plotted are critical He concentrations per unit area required to observe He bubbles in TEM for these three interfaces as well as the areal densities of MDIs computed using O-lattice theory[41] for a wide range of lattice parameter ratios at interfaces with the same crystallographic character as those investigated here. These three sets of data are nearly proportional to each other, in agreement with the hypothesis that the areal density of MDIs determines the conditions at which the platelet-to-bubble transition occurs at different interfaces.

The proportionality factor between the critical He concentration found by TEM and the areal density of MDIs is the critical number of He atoms per MDI at which the platelet-to-bubble transition occurs. The data in Fig. 5 indicate that this critical number is 25 He atoms, in good agreement with multiscale modeling, which predicts a critical number of 21 He atoms.[22] The proportionality factor between the reduced critical fluence required to detect Cu_{LD} layers in NR and the critical He concentration required to observe He bubbles in TEM is the fraction of He atoms implanted into fcc-bcc bilayers that eventually becomes trapped at fcc-bcc interfaces. The remainder of the He implanted into the bilayers may diffuse to trapping sites other than the fcc-bcc interface (such as vacancies or dislocations), to the free surface, and to the interface with the substrate.

No prior information is available concerning the fraction of He implanted into the bilayers that eventually ends up at fcc-bcc interfaces, so we infer it to be 38% ± 14% using the data in Fig. 5. If there had been no distributed sinks such as vacancies and dislocations in the bilayers, then implanted He could only diffuse to free surfaces, fcc-bcc interfaces, and bilayer-substrate interfaces, giving a 50% expected fraction of implanted He that eventually becomes trapped at fcc-bcc interfaces. This value is reasonably close to the inferred fraction of 38%, confirming that the interpretation of the NR and TEM data are consistent with each other. The fact that the inferred He trapping fraction is lower than 50% gives indirect evidence of the presence of distributed sinks in the bilayers. Additionally, previous investigations that compared depth profiles of low energy implanted He computed by SRIM with ones measured by nuclear reaction analysis (NRA) concluded that the former tended to underpredict the implantation depth,[4,16] providing anther possible cause of the low value of the inferred He trapping fraction.

The critical concentrations of He required for forming interface bubbles estimated from NR and TEM data show qualitative agreement with each other. The disparities observed between the two sets of data may be explained on the basis of differences in the fraction of He that is ultimately trapped at each fcc-bcc interface. The data in Fig. 5 suggest that the fraction of He trapped at the Cu-Nb interface is actually lower than the inferred value of 38%. Such variation is to be expected since each bcc metal that forms the interface responds differently to He implantation. Under implantation, the concentration of vacancies generated in the bcc layer and the mobility of He-vacancy complexes are governed by the properties of the bcc layer. Both of these quantities influence the fraction of He that may diffuse to the fcc-bcc interface and get trapped there.

C. Variation of bubble size with implanted He fluence in Cu-Nb interfaces

The decrease in mass density of Cu_{LD} layers measured by NR above the critical implanted He fluence at Cu-Nb interfaces may be used to estimate the volume of interfacial He bubbles. Assuming that the SLD of bubbles is zero and that there is one bubble at each MDI, we use the rule of mixtures to estimate the upper bound on the volume per He bubble at each He fluence above the threshold value. We then compare these values to equilibrium volumes of He-filled cavities at Cu-Nb interfaces calculated using a reaction-diffusion model described elsewhere.[22] The model requires the number of He atoms per bubble to be specified and is solved using the finite element method (FEM).

With increasing He fluence, increasing numbers of He atoms are trapped in interface bubbles. The volume of the bubbles then increases to accommodate the higher pressure of the He trapped inside them. We use the fraction of implanted He that eventually ends up at fcc-bcc interfaces inferred in Sec. IV B to estimate how many He atoms are inside each bubble at any given total fluence. A comparison between the inferred and calculated He bubble volumes is presented as a function of the number of He atoms trapped in
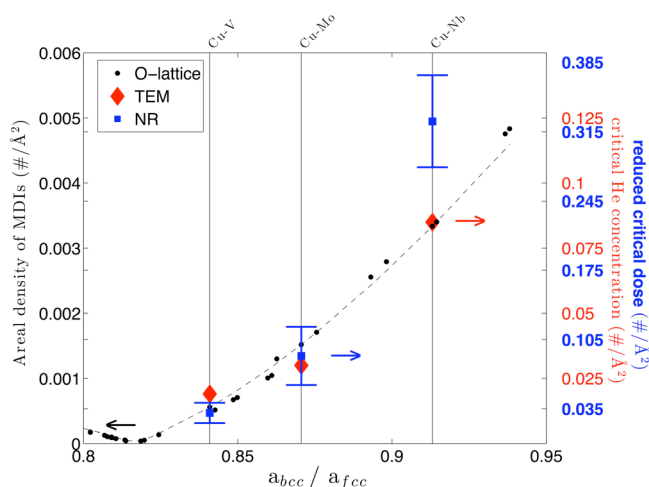

FIG. 5. Blue squares show the reduced critical fluence required to measure a decrease in interfacial Cu density using NR as a function of lattice parameter ratio for Cu-Nb, Cu-Mo, and Cu-V interfaces. Red diamonds are critical interfacial He concentrations required to observe He bubbles in TEM. Black dots are areal densities of MDIs calculated using O-lattice theory and the dashed line is a guide to the eye.[21]
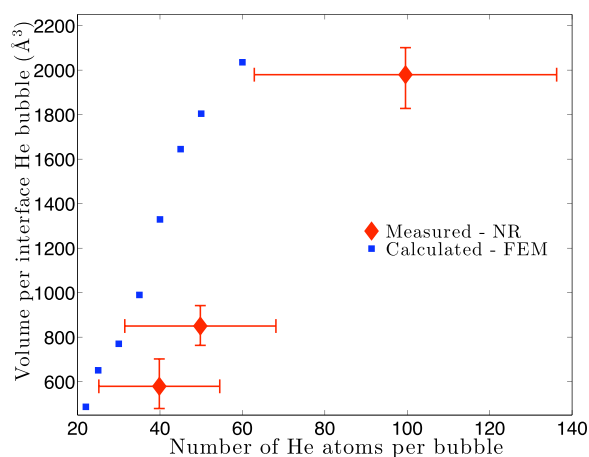
FIG. 6. Red diamonds show the volume per He bubble at Cu-Nb interfaces determined as a function of the number of He atoms estimated from NR measurements. Blue squares represent volumes of stable interfacial He bubbles calculated from a reaction-diffusion model using FEM.

each bubble in Figure 6. These two determinations of He bubble volume are in reasonable agreement with each other and show the same trends with increasing number of He atoms, validating our conclusion that He bubble formation is responsible for the decrease in the mass density of Cu adjacent to fcc-bcc interfaces.

As pointed out in Sec. IV B, the number of He atoms implanted into the Cu-Nb bilayer that eventually become trapped at Cu-Nb interfaces may be smaller than the value of 38% inferred from Fig. 5. If this conclusion is correct, then the red data points in Fig. 6 should be shifted somewhat to the left, yielding a smaller discrepancy with respect to the FEM calculations.

V. DISCUSSION

The NR measurements on He implanted fcc-bcc semi-coherent interfaces described here provide direct evidence of the He "platelet-to-bubble" transformation predicted by previous multiscale modeling efforts.[22] Below a critical He fluence, He atoms are trapped in stable, nanometer-scale platelets that are below the resolution limit of NR and therefore do not alter the measured reflectivity profiles. Above a critical He fluence, the platelets transform to approximately spherical bubbles with volumes nearly three times as large as those of the platelets. These bubbles are detected by NR as low-density Cu layers, Cu_{LD}, adjacent to the fcc-bcc interfaces. The fact that the Cu_{LD} layers do not form gradually, but rather only once a critical fluence is exceeded provides strong evidence of the platelet-to-bubble transformation, which is also a discrete threshold phenomenon.

This work also reinforces the importance of misfit dislocation networks in determining how He interacts with semi-coherent interfaces. MDIs are trapping sites for He atoms and the density of such sites controls how much He may be stably stored at interfaces. Other semi-coherent interfaces containing misfit dislocations besides the fcc-bcc interfaces investigated here may also trap He at MDIs. For example, He bubbles nucleate preferentially at nodal points in the screw dislocation networks of twist grain boundaries in

Au,[42] Fe,[43] and Cu.[44] Is the formation of He bubbles at these grain boundaries also preceded by the formation of stable He platelets?

Since interfacial He platelets store He nearly three times more efficiently than bubbles, as shown in Ref. 22, their formation at interfaces may have important consequences for the design of He damage-resistant structural materials for future fusion and advanced fission reactors. For example, by creating materials containing interfaces with high densities of MDIs, it may be possible to delay the platelet-to-bubble transformation and thereby maximize the concentration of He required to nucleate bubbles. More detailed control over interfacial MDI distributions may allow He platelets and bubbles to be patterned, for example, into connected channels that allow for continuous He outgassing.

Our work demonstrated the need for better understanding of processes influencing the trapping and diffusion of He implanted into single crystals. Such understanding would have allowed for a more quantitative analysis of the data in Figs. 5 and 6, as argued in Secs. IV B and IV C. Kinetic Monte Carlo simulations parameterized by defect formation and migration data obtained from first principles simulations may yield such information.

This study also shows that NR is a powerful tool for resolving nano-scale features at buried solid-state interfaces. The high spatial resolution of this technique may also be applied to study other forms of damage at interfaces, such as morphological evolution under heavy-ion bombardment, radiation-induced segregation, or hydride formation. NR may also be used to validate atomistic modeling predictions.

Finally, the results of the work presented here indicate how modeling studies may be used to inform the design of experiments for hypotheses testing. By combining results from TEM and NR experiments with hypotheses obtained through modeling, we were able to obtain quantitative insights into the behavior of interface-He interactions at fcc-bcc semi-coherent interfaces and relate He trapping to interface structure. Design of experiments specifically for testing of hypotheses developed by accurate modeling is a means to deeper integration of computational modeling and experimental investigations.

[1]H. Ullmaier, Nucl. Fusion **24**, 1039 (1984).
[2]S. J. Zinkle, Fusion Eng. Des. **74**, 31 (2005).
[3]J. Laakmann, P. Jung, and W. Uelhoff, Acta Metall. **35**, 2063 (1987).
[4]D. Bhattacharyya, M. J. Demkowicz, Y. Q. Wang, R. E. Baumer, M. Nastasi, and A. Misra, Microsc. Microanal. **18**, 152 (2012).

[5] K. Russell, Acta Metall. **26**, 1615 (1978).

[6] K. Farrell, Radiat. Eff. Defects Solids **53**, 175 (1980).

[7] S. J. Zinkle, W. G. Wolfer, and G. Kulcinski, Philos. Mag. A **55**, 127 (1987).

[8] H. Trinkaus and H. Ullmaier, J. Nucl. Mater. **212–215**, 303 (1994).

[9] H. Schroeder, W. Kesternich, and H. Ullmaier, Nucl. Eng. Des. Fusion **2**, 65 (1985).

[10] D. N. Braski, H. Schroeder, and H. Ullmaier, J. Nucl. Mater. **83**, 265 (1979).

[11] W. Coghlan and L. K. Mansur, J. Nucl. Mater. **122–123**, 495 (1984).

[12] R. E. Stoller and G. R. Odette, J. Nucl. Mater. **122–123**, 514 (1984).

[13] L. K. Mansur, E. H. Lee, and P. J. Maziasz, J. Nucl. Mater. **141–143**, 633 (1986).

[14] G. R. Odette, M. J. Alinger, and B. D. Wirth, Annu. Rev. Mater. Res. **38**, 471 (2008).

[15] G. R. Odette and D. T. Hoelzer, JOM **62**, 84 (2010).

[16] M. J. Demkowicz, D. Bhattacharyya, I. Usov, Y. Q. Wang, M. Nastasi, and A. Misra, Appl. Phys. Lett. **97**, 161903 (2010).

[17] E. G. Fu, A. Misra, H. Wang, L. Shao, and X. Zhang, J. Nucl. Mater. **407**, 178 (2010).

[18] N. Li, J. J. Carter, A. Misra, L. Shao, H. Wang, and X. Zhang, Philos. Mag. Lett. **91**, 18 (2011).

[19] M. J. Demkowicz, R. G. Hoagland, and J. P. Hirth, Phys. Rev. Lett. **100**, 136102 (2008).

[20] M. J. Demkowicz, J. Wang, and R. G. Hoagland, in *Dislocations in Solids*, edited by J. P. Hirth (Elsevier, Amsterdam, 2008), Vol. 14, p. 141.

[21] M. J. Demkowicz, A. Misra, and A. J. Caro, Curr. Opin. Solid State Mater. Sci. **16**, 101 (2012).

[22] A. Kashinath, A. Misra, and M. J. Demkowicz, Phys. Rev. Lett. **110**, 086101 (2013).

[23] M. Zhernenkov, M. S. Jablin, A. Misra, M. Nastasi, Y. Q. Wang, M. J. Demkowicz, J. K. Baldwin, and J. Majewski, Appl. Phys. Lett. **98**, 241913 (2011).

[24] J. L'Ecuyer, J. Appl. Phys. **47**, 381 (1976).

[25] J. L. Flament, F. Ziélinski, S. Saudé, and R. I. Grynszpan, Nucl. Instrum. Methods Phys. Res. B **216**, 161 (2004).

[26] T. E. Mitchell, Y. C. Lu, and M. Nastasi, J. Am. Ceram. Soc. **80**, 1673 (1997).

[27] J. F. Ziegler, J. P. Biersack, and M. D. Ziegler, *Stopping and Range of Ions in Matter* (Pergamon Press, New York, 1985).

[28] M. Dubey, M. S. Jablin, P. Wang, M. Mocko, and J. Majewski, Eur. Phys. J. Plus **126**, 110 (2011).

[29] V. F. Sears, "Thermal-neutron scattering lengths and cross sections for condensed-matter research," Atomic Energy of Canada Limited Report AECL-8490 (1984).

[30] V. F. Sears, Neutron News **3**, 26 (1992).

[31] O. S. Heavens, *Optical Properties of Thin Solid Films* (Butterworths Scientific Publications, London, 1955).

[32] F. Abelès, J. Phys. Radium **11**, 307 (1950).

[33] A. Nelson, J. Appl. Crystallogr. **39**, 273 (2006).

[34] K. Pearson, Philos. Mag. **50**, 157 (1900).

[35] A. Y. Dunn, M. G. McPhie, L. Capolungo, E. Martinez, and M. Cherkaoui, J. Nucl. Mater. **435**, 141 (2013).

[36] M. A. Nastasi, J. W. Mayer, and J. K. Hirvonen, *Ion-solid Interactions: Fundamentals and Applications* (Cambridge University Press, Cambridge, 1996).

[37] A. Misra, M. J. Demkowicz, X. Zhang, and R. G. Hoagland, JOM **59**, 62 (2007).

[38] T. Hochbauer, A. Misra, K. Hattar, and R. G. Hoagland, J. Appl. Phys. **98**, 123516 (2005).

[39] R. S. Averback, D. Peak, and L. J. Thompson, Appl. Phys. A **39**, 59 (1986).

[40] K. Hattar, M. J. Demkowicz, A. Misra, I. M. Robertson, and R. G. Hoagland, Scr. Mater. **58**, 541 (2008).

[41] W. Bollmann, *Crystal Defects and Crystalline Interfaces* (Springer Verlag, 1970).

[42] Z. Di, X. M. Bai, Q. Wei, J. Won, R. G. Hoagland, Y. Q. Wang, A. Misra, B. P. Uberuaga, and M. Nastasi, Phys. Rev. B **84**, 052101 (2011).

[43] J. Hetherly, E. Martinez, M. Nastasi, and A. Caro, J. Nucl. Mater. **419**, 201 (2011).

[44] J. Hetherly, E. Martinez, Z. F. Di, M. Nastasi, and A. Caro, Scr. Mater. **66**, 17 (2012).